PHYSICAL SCIENCES

Efficient energy transfer in a hybrid organic-inorganic van der Waals heterostructure

Xiaoqing Chen[1,2]†, Huijuan Zhao[3]†, Ruixiang Fei[4,5], Chun Huang[6], Jingsi Qiao[6], Cheng Sun[7], Haiming Zhu[7], Li Zhan[1], Zehua Hu[1], Songlin Li[1], Li Yang[4], Zemin Tang[3], Lianhui Wang[3], Yi Shi[1], Wei Ji[8], Jian-Bin Xu[9], Li Gao[3,10]*, Xuetao Gan[2]*, Xinran Wang[1,11,12]*

Two-dimensional (2D) materials offer strong light-matter interaction and design flexibility beyond bulk semiconductors, but an intrinsic limit is the low absorption imposed by the atomic thickness. A long-sought-after goal is to achieve complementary absorption enhancement through energy transfer (ET) to break this limit. However, it is found challenging due to the competing charge transfer (CT) process and lack of resonance in exciton states. Here, we report highly efficient ET in a 2D hybrid organic-inorganic heterostructure (HOIST) of Me-PTCDI/WS_2. Resonant ET is observed leading to enhanced WS_2 photoluminescence (PL) by 124 times. We identify Dexter exchange between the Frenkel state in donor and an excited 2*s* state in acceptor as the main ET mechanism, as supported by density functional theory calculations. We further demonstrate ET-enhanced phototransistor devices with enhanced responsivity by nearly 1000 times without sacrificing the response time. Our results expand the understanding of interlayer relaxation processes in 2D materials and open opportunities in optoelectronic devices.

INTRODUCTION

Stacking atomically thin two-dimensional (2D) materials into van der Waals (vdW) heterostructures can form artificial quantum materials where interlayer charge or energy relaxation processes lead to new physics and devices (*1*–*5*). However, for optoelectronic applications, a fundamental limit of 2D materials is the low absorption due to the atomic thickness. To overcome this fundamental limit, a promising approach is to create a heterointerface with complementary photosensitive materials (donors) and harvest the excitations therein (*6*–*16*). The interlayer relaxation process mainly consists of two competing pathways. The first pathway is charge transfer (CT) due to the built-in electrical potential, which has been the dominating process due to the ultrashort time constant ~50 fs (*17*, *18*). However, the separation of electrons and holes leads to quenching of photo- and electroluminescence and substantially elongated device response time due to traps at the heterointerface, which is a common issue in CT-enhanced optoelectronic devices (*9*–*11*). The second pathway is energy transfer (ET), which refers to nonradiative transfer of excitations in the form of excitons (*12*–*16*). Compared to CT, ET can avoid the effect of interface traps and is desirable for ultrafast devices. However, it has been proved very challenging to achieve efficient ET in 2D heterostructures due to the competing CT process (*12*), spatial separation of donor and acceptor (*14*, *15*), or difficulties in realizing donor-acceptor resonance (*19*). In addition, for inorganic vdW heterostructures, the interlayer overlap of excitonic wave functions is small because they are mainly composed of localized *d*-orbitals confined within the plane (*20*).

On the other hand, integrating organic molecules into vdW heterostructures can vastly expand the existing functionalities owing to the complementary properties and chemical tunability at molecular level (*19*, *21*–*29*). In particular, many molecular dyes host localized Frenkel excitons with large oscillator strength and photoluminescence (PL) quantum yield. They can be assembled into layered crystalline films on many 2D materials to form hybrid organic-inorganic heterostructure (HOIST) (*27*–*31*). Now, ET in diverse HOISTs has been explored but with low ET enhancement limited to several times (table S1). Here, we exploit the unique properties of organic dye molecules and demonstrate highly efficient ET to 2D semiconductors, enabled by the resonantly coupling of Frenkel exciton in dimethyl-3,4,9,10-perylenete- tracarboxilic diimide (Me-PTCDI) molecular crystal and Wannier-Mott exciton in WS_2. The ET is manifested by shortening of lifetime in the donor and simultaneous enhancement of PL intensity (by as much as 124 times) and optical anisotropy in the acceptor. Density functional theory (DFT) calculations show that the ET rate is more than one order of magnitude higher than pure inorganic heterostructures due to the reduced interlayer spacing and spatial delocalization of the 2*s* state. By harvesting ET, we break the limit of far-field absorption in 2D semiconductors and demonstrate ET-enhanced phototransistor devices without sacrificing the operation speed.

[1]National Laboratory of Solid State Microstructures, School of Electronic Science and Engineering and Collaborative Innovation Center of Advanced Microstructures, Nanjing University, Nanjing 210093, China. [2]Key Laboratory of Light Field Manipulation and Information Acquisition, Ministry of Industry and Information Technology, and Shaanxi Key Laboratory of Optical Information Technology, School of Physical Science and Technology, Northwestern Polytechnical University, Xi'an 710129, China. [3]State Key Laboratory of Flexible Electronics, School of Materials Science and Engineering, Nanjing University of Posts and Telecommunications, Nanjing 210023, China. [4]Department of Physics, Washington University in St Louis, St Louis, MO 63130, United States. [5]Key Lab of Advanced Optoelectronic Quantum Architecture and Measurement (Ministry of Education), Beijing Key Lab of Nanophotonics & Ultrafine Optoelectronic Systems and School of Physics, Beijing Institute of Technology, Beijing 100081, China. [6]School of Integrated Circuits and Electronics & Advanced Research Institute of Multidisciplinary Sciences, Beijing Institute of Technology, Beijing 100081, China. [7]Key Laboratory of Excited - State Materials of Zhejiang Province, Department of Chemistry, Zhejiang University, Hangzhou, 310027, China. [8]Department of Physics and Beijing Key Laboratory of Optoelectronic Functional Materials and Micro-Nano Devices, Renmin University of China, Beijing 100872, China. [9]Department of Electronic Engineering, The Chinese University of Hong Kong, Shatin, N.T., Hong Kong SAR, P. R. China. [10]School of Science, Nanjing University of Posts and Telecommunications, Nanjing 210023, China. [11]School of Integrated Circuits, Nanjing University, Suzhou 215163, China. [12]Suzhou Laboratory, Suzhou, China.
*Corresponding author. Email: iamlgao@njupt.edu.cn (L.G.); xuetaogan@nwpu.edu.cn (X.G.); xrwang@nju.edu.cn (X.W.)
†These authors contributed equally to this work.

RESULTS

Our HOIST consists of Me-PTCDI molecular crystal and WS_2 (both are monolayers; see fig. S1) sandwiched by hexagonal boron nitride (h-BN) on both sides (Fig. 1, A and B). The samples were fabricated by vapor phase transport growth of Me-PTCDI on h-BN (*30*) with high thickness uniformity (fig. S2), followed by sequential dry transfer of exfoliated WS_2 and top h-BN flake. The high-quality interface between Me-PTCDI and WS_2 was further verified by high-resolution cross-sectional transmission electron microscope (TEM) with interlayer distance of ~493 pm (see fig. S3) The optical measurements were carried out in an optical cryostat at 77 K, unless otherwise stated (details of sample fabrication and measurements are described in Materials and Methods). The differential reflectance of the HOIST showed several well-defined resonances from Me-PTCDI and WS_2 (fig. S4), which confirmed that the optical properties of the individual layers and the molecular packing were preserved. Figure 1D plots the derivative of reflectance contrast of WS_2. We observed all the major resonance features, including neutral (X^0) and charged (X^-) A excitons, excited states (2*s* and 3*s*) and B exciton (*32*). A unique feature of the HOIST is that the Frenkel exciton in Me-PTCDI is energetically resonant with the first excited (2*s*) state of A exciton in WS_2 (Fig. 1D and fig. S4). Besides, the ground states are quite close in the HOIST, which facilitates the excitons in Me-PTCDI transferring into WS_2 (Fig. 1C, note S1, and fig. S5). Figure 1E plots the PL spectrum of a typical HOIST, together with the isolated WS_2 and Me-PTCDI regions from the same sample. We observed simultaneous enhancement of WS_2 emission (by ~50 times) and quenching of Me-PTCDI (by ~73%) in the heterostructure, which was strong evidence of ET (*6*–*8*). The brightening of WS_2 in the HOIST was also evident from PL image (Fig. 1B), which was distinct from PL quenching in typical vdW heterostructures (*17*, *18*, *33*).

We further investigated ET by PL excitation (PLE) spectroscopy. Figure 2A plots the PLE intensity maps of WS_2 and HOIST, respectively, from the same sample. The WS_2 showed weak PL emission from X^0 (2.075 eV) and X^- (2.05 eV), with enhanced response when excited at A and B excitons. The HOIST, in contrast, showed a new dominant excitation peak at ~2.24 eV, corresponding to the Frenkel exciton of Me-PTCDI. This peak was attributed to ET from the Me-PTCDI donor. Under the resonant excitation of Me-PTCDI, the PL of WS_2 was significantly broadened and red-shifted compared to the nonheterostructure region (Figs. 1E and 2A), which was possibly due to interaction effects at high exciton density (*34*, *35*). Another possible explanation of the new peak was the transfer of photo-induced carriers (photodoping) by Me-PTCDI to influence the PL of WS_2. However, this scenario was ruled out because the X^-/X^0 ratio remained nearly constant across multiple excitation energies, which was inconsistent with photodoping (fig. S6) (*12*). The absence of strong ET in HOIST consisting of multilayer Me-PTCDI (although it has stronger optical absorption) also suggested that CT was not the dominant process (fig. S7). The weak CT was further supported by the band structure of the heterostructure characterized experimentally. As shown in Fig. 1C, the conduction band minimum (valance band maximum) of WS_2 is energetically very close to the electron affinity (ionization potential) of Me-PTCDI, which is not expected to generate strong built-in field and CT.

Figure 2B shows quantitative comparison of the PLE of HOIST and WS_2 (derived from horizontal line cuts in Fig. 2A). The PL enhancement had two contributions. The first was the overall enhancement

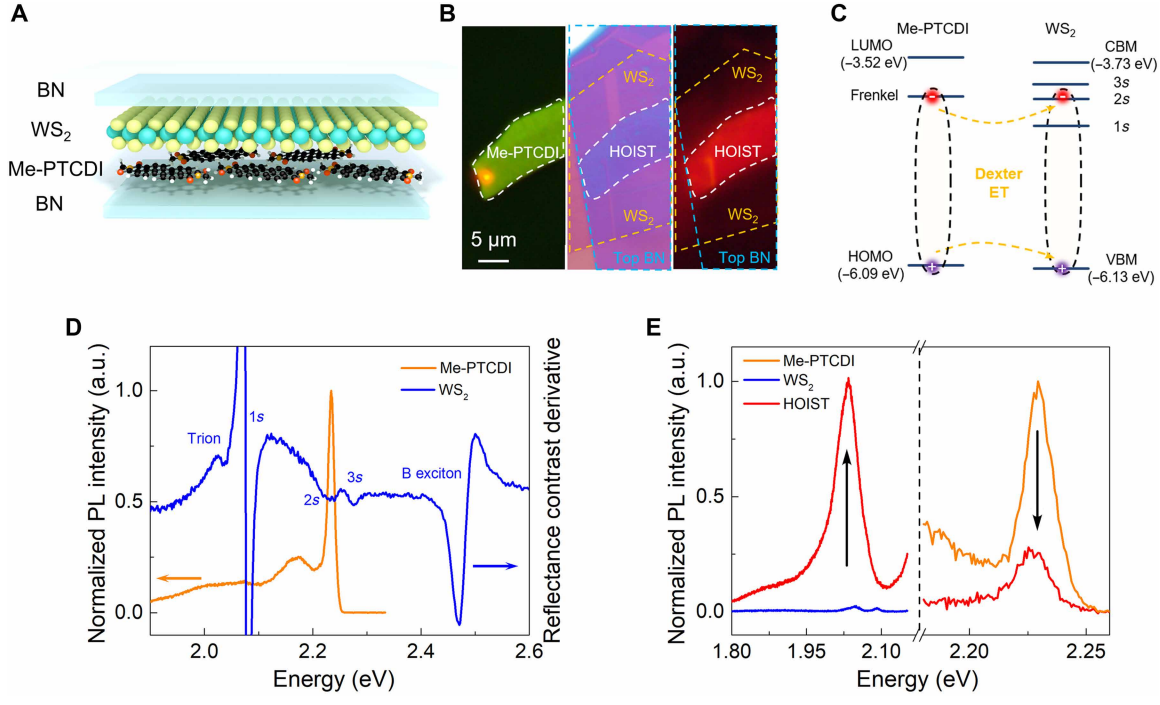

Fig. 1. Me-PTCDI-WS_2 HOIST. (**A**) Schematic illustration of the sample structure. (**B**) PL image of Me-PTCDI on h-BN before transferring WS_2 on top (left, 300 K), optical micrograph (middle, 300 K), and PL image (right, 77 K) of HOIST. Scale bar, 5 μm. (**C**) Band structure of HOIST and the Dexter ET process. (**D**) Derivative of reflection contrast of WS_2 (blue) and PL spectrum of Me-PTCDI (orange), both measured at 77 K. (**E**) PL spectra of WS_2 (left) and Me-PTCDI (right) in heterostructure and nonheterostructure regions from the same sample. The left and right panels are excited with 2.24- and 2.33-eV laser, respectively. a.u., arbitrary unit.

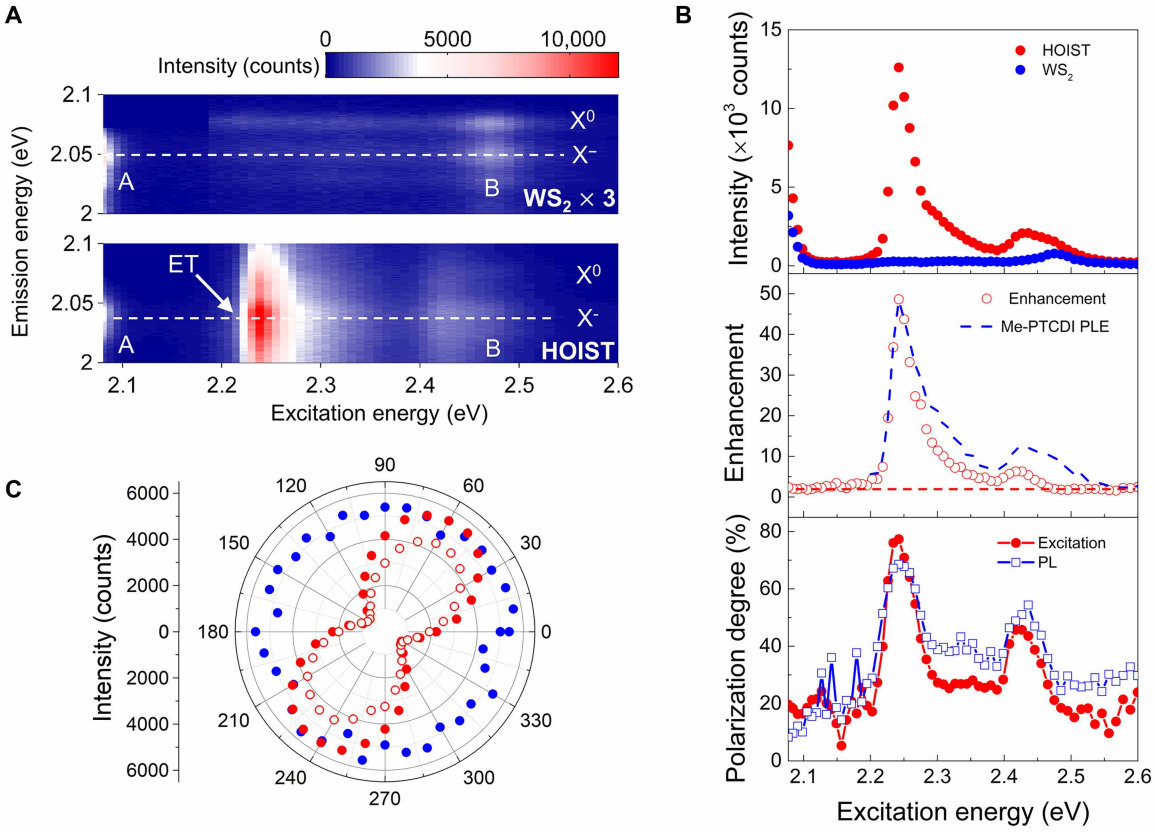

Fig. 2. Optical spectroscopy of HOIST. (**A**) PLE of WS_2 (top, intensity multiplied by three times) and HOIST (bottom). (**B**) Top: PL intensity of X^- as a function of excitation energy in WS_2 and HOIST, obtained from the horizontal dashed line cuts from (A); Middle: PL enhancement factor derived from (B) (red open symbols) overlapping with PLE intensity of Me-PTCDI (blue dashed line). Bottom: Degree of polarization in excitation (solid symbols) and emission (open symbols) as a function of excitation energy. (**C**) Polar plot of PL intensity of WS_2 X^- in HOIST as a function of excitation polarization angle (red solid circles) and emission polarization angle (red open symbol) with the excitation polarization angle where ET effect is strongest. The blue solid circles give the PL intensity of pristine WS_2 X^- as a function of excitation polarization angle (×50 for clarity).

due to the change in PL quantum yield with the h-BN encapsulation (the red dashed baseline in Fig. 2B, middle) (*36*) independent of excitation. The second (and main) contribution was from ET, with distinct optical signatures of Me-PTCDI. Consequently, the overall enhancement followed the spectral response of Me-PTCDI and reached ~48 times under resonant excitation (Fig. 2B, middle). After subtracting the effect of h-BN encapsulation, we calculated that the monochromatic (at 2.24 eV) and broadband (from 2.07 to 2.6 eV, covering both A and B excitons) absorption of WS_2 was increased by ~20 and ~2.5 times, respectively, via ET. The large PL enhancement was reproducible among multiple samples with the highest enhancement factor reaching ~124 times, which is the highest compared with the type I CT and fluorescence resonance energy transfer (FRET) (fig. S8 and table S1). Because of the giant oscillation strength of the Frenkel excitons in the monolayer Me-PTCDI, the ET performance of the HOIST can exceed the HOISTs using bulk organic layers for almost two orders of magnitude (*37*, *38*).

Besides enhanced PL intensity, ET also caused optical anisotropy in WS_2. Isolated WS_2 did not exhibit linear anisotropy in PL (Fig. 2C, blue solid circles) (*39*). In the HOIST, however, both PL and excitation of WS_2 were highly anisotropic (Fig. 2C, red solid and open circles; see Materials and Methods for measurement details). The polarization angle was consistent with the PL of Me-PTCDI donor and independent of excitation polarization angle (fig. S9), and the degree of polarization, $P = \frac{I_{max} - I_{min}}{I_{max} + I_{min}}$, reached 77% at resonant excitation. The anisotropic behavior was most distinct at the absorption peaks of Me-PTCDI (Fig. 2B, bottom). Because the absorption of WS_2 keeps isotropic in the HOIST (fig. S10), the strong exciton excitation polarization of WS_2 indicates that the absorption of HOIST is mainly from Me-PTCDI through ET when resonant with Me-PTCDI. The relationship between the enhancement factor and the excitation polarization angle can be well fitted with $c * \cos^2\left(\frac{x-a}{180} * \pi\right) + b$, where a is the molecular crystal orientation angle, b represents the change in the quantum yield of PL in WS_2 due to the doping effect, c is the maximum enhancement factor due to ET (fig. S11). The observed PL polarization behavior indicated that electrons and holes are transferred into WS_2 coherently, i.e., it preserved the exciton dipole moment of the donor. The excitons transferred into WS_2 are finally relaxed to trions that simultaneously excite both −K and + K valleys and transfer the optical coherence to valley quantum coherence (fig. S12). Our observation was fundamentally distinct from the separation of electron-hole pairs and subsequent CT in type-I heterostructures, which was incoherent and would give isotropic PL emission (*13*, *16*). The ability to control the polarization behavior in monolayer transition metal dichalcogenides (TMDCs) could also

open new possibilities toward coherent manipulation of valley degree of freedom (*40*).

The ET was further corroborated by transient absorption spectroscopy (note S2 and fig. S13). The Me-PTCDI in the nonheterostructure region showed lifetime $\tau_{\text{Me-PTCDI}} \sim 1.6$ ps (fig. S14), which was approximately the radiative lifetime τ_r as the nonradiative lifetime in monolayer Me-PTCDI was much longer (*30*). This ultrashort radiative lifetime is related to the super-radiance in J aggregates owing to the large unscreened dipole interactions and suppression of CT process in the monolayer Me-PTCDI (*30*). Because of the extra ET process, $\tau_{\text{Me-PTCDI}}$ was expected to shorten in the HOIST, which was confirmed by our pump-probe measurements (fig. S14). Meanwhile, the dynamics of WS_2 keeps unchanged, which excludes the CT effect (fig. S15). Assuming that ET is the primary nonradiative process in the Me-PTCDI donor, the total decay rate can be written as $k_{\text{Me-PTCDI}} = \frac{1}{\tau_{\text{Me-PTCDI}}} = k_r + k_{ET}$, where $k_r = \frac{1}{\tau_r}$ and $k_{ET} = \frac{1}{\tau_{ET}}$ are radiative recombination and ET rate, respectively. By subtracting k_r, we obtained $\tau_{ET} = 3.1$ ps, corresponding to ET efficiency $(\frac{k_{ET}}{k_{\text{Me-PTCDI}}}) \sim 34\%$, which is close to the maximum ET efficiency through PL quenching of 73%. The discrepancy between the two estimated ET efficiencies is attributed to the additional many-body effects such as the exciton-exciton annihilation under pulsed laser, which will compete with the ET process (*41*).

Next, we discuss the ET mechanism in our HOIST. ET is nonradiative transfer of excitations in the form of excitons, mediated by either short-range electron exchange (Dexter) (*42*) or long-range dipole interactions (FRET) (*43*). The nature of FRET requires large oscillation strength for both the donor and acceptor states, and physical separation in the range of 1 to 10 nm (*44*). Dexter, on the other hand, depends on the wave function overlap and is not limited by the oscillator strength of the states. FRET is unlikely in our HOIST because the interlayer spacing is much less than 1 nm (Fig. 3A), and the oscillator strength of WS_2 2*s* state is very small (fig. S16) (*45*). The spin conservation law also plays a key role in the ET process. Despite the nonemissive nature of the 2*s* state in WS_2, it can be resolved from the absorption spectrum, which indicates that a singlet-singlet ET can be supported between Me-PTCDI and WS_2 (*42*). To elucidate the mechanism, three control experiments were performed. First, we fabricated HOIST using monolayer $MoSe_2$ as the acceptor, which would give more efficient ET under FRET mechanism due to higher absorption at the Me-PTCDI emission energy (fig. S17) (*46*). Second, we separated Me-PTCDI and WS_2 by a layer of h-BN, whose thickness was well within the range of Förster dipole interactions (figs. S18 and S19). Only radiative ET with low efficiency is observed, which rules out FRET and suggests Dexter exchange as the ET mechanism. Third, the efficiency of FRET drops with the decrease of temperature. However, the ET enhancement in HOIST reaches the maximum at 77 K when the temperature decreases from room temperature to 4 K (figs. S20 and S21), which is due to the match of energy levels of 2*s* state of WS_2 and Frenkel states of Me-PTCDI. In addition, we numerically simulate the FRET rate in the HOIST, which generates τ_{FRET} of 105.4 ns (see note S3). This value is five orders of magnitude longer than the measured ET time ruling out the FRET mechanism.

For Dexter exchange, the ET rate can be written as (*47*)

$$k_{ET} = KJ_{\text{norm}}e^{\left(-\frac{2d}{L}\right)} \quad (1)$$

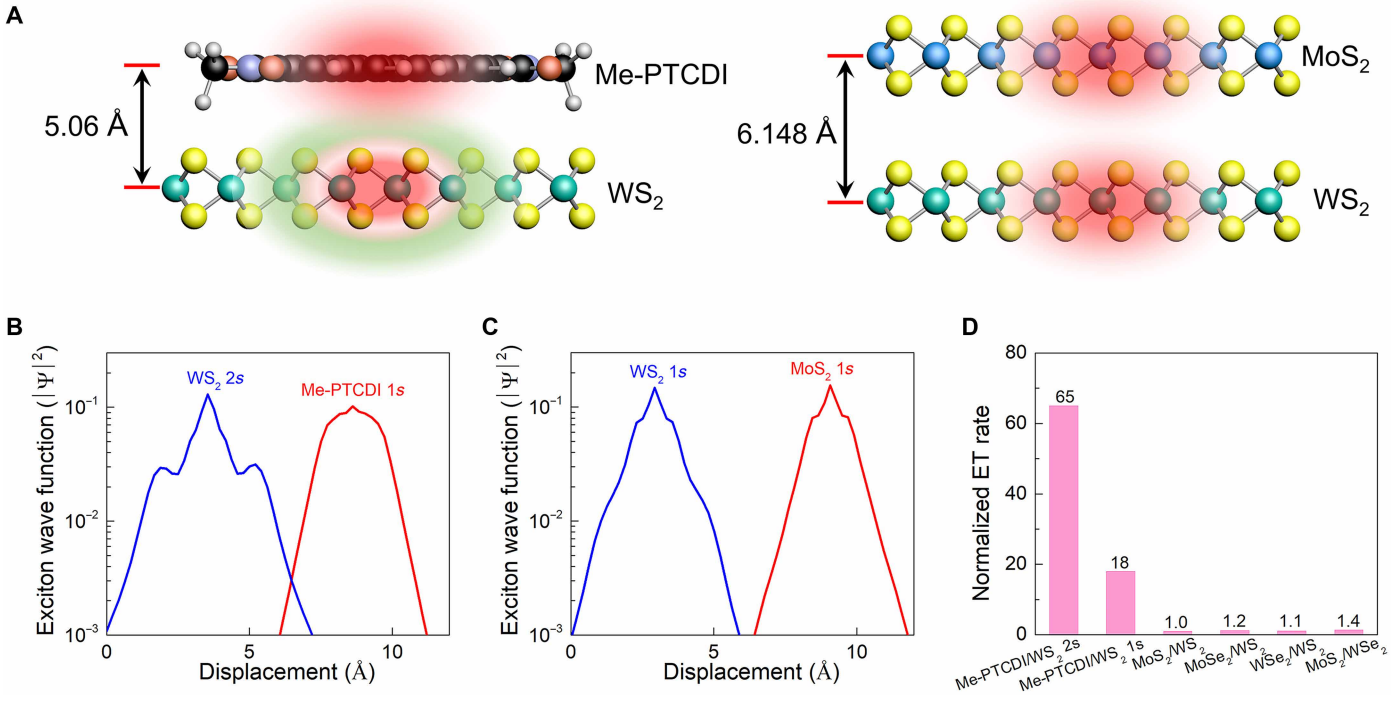

Fig. 3. Theoretical calculations of exciton wavefunction and ET rates. (**A**) Illustration of interlayer distance and exciton wave functions in HOIST (left) and MoS_2/WS_2 heterostructure (right). (**B** and **C**) Out-of-plane distribution of exciton wave functions in HOIST (B) and MoS_2/WS_2 heterostructure (C). (**D**) Normalized ET rates in different 2D heterostructures. For Me-PTCDI/WS_2 HOIST, we use 1*s* states in Me-PTCDI and consider both 1*s* and 2*s* states in WS_2. For MoS_2/WS_2, $MoSe_2/WS_2$, WSe_2/WS_2, and MoS_2/WSe_2 heterostructures, 1*s* states are used.

where K is a prefactor related to the excitonic orbital interactions, J_{norm} is the normalized spectral overlap, $d$is the center-to-center distance between the donor and the acceptor, and L is the characteristic wave function decay length (e.g., vdW radius). Our HOIST has two unique advantages compared to inorganic vdW heterostructures (e.g., MoS_2/WS_2). First, DFT calculations showed that the interlayer center-to-center distance d of HOIST (5.06 Å) was significantly smaller than that of the MoS_2/WS_2 (6.15 Å; Fig. 3A), leading to enhanced wave function overlaps. This was indeed observed in similar HOIST composed of PTCDA and WSe_2 (*26*). Second, the 2*s* state of WS_2 was more spatially extended in the out-of-plane direction than its ground state due to the reduced effective dielectric screening (Fig. 3, B and C) (*32*). Both factors contributed to the increased k_{ET} according to Eq. 1. DFT calculations show that the wave function overlap mainly through the p_z orbitals of S and C atom (figs. S22 and S23). For quantitative comparison, we calculated k_{ET} of six combinations using Fermi golden rule (see Materials and Methods) (*48*, *49*). The results are summarized in Fig. 3D (normalized by k_{ET} of MoS_2/WS_2 1*s* states). We can see that the k_{ET} of all the inorganic TMDC heterostructures is close to 1, but substituting MoS_2 with Me-PTCDI markedly increases the k_{ET} to 18 due to reduced interlayer distance. The k_{ET} is further increased to 65 with 2*s* state of WS_2. The variation of k_{ET} is consistent with the orbital wave function overlap, which is sensitive to the interlayer distance (fig. S23 and table S2). Our theoretical calculations suggest that the ET is most likely between the resonant 1*s* Frenkel exciton of Me-PTCDI and 2*s* Wannier-Mott exciton of WS_2 (fig. 1C).

The observed ET allows the simultaneous transfer of electron-hole pairs to TMDCs within picosecond timescale, which could enable ultrafast broadband optoelectronic devices. To this end, we fabricated Me-PTCDI/WS_2 HOIST phototransistors as shown in Fig. 4 (see Materials and Methods for fabrication details). We first carried out photocurrent (I_{ph}) mapping using laser excitations in resonance with WS_2 A exciton (2.052 eV), where no ET was expected. We observed photoresponse only near the drain electrode where the contact band bending facilitates electron-hole separation and little difference between the HOIST and WS_2 regions (Fig. 4D, top). We then switched the laser energy in resonance with the Me-PTCDI Frenkel exciton (2.254 eV; Fig. 4D, bottom). We observed huge I_{ph} enhancement in the HOIST region due to ET. The I_{ph} of HOIST was higher than WS_2 across a wide range of V_g (Fig. 4F). At $V_g = -22$ V (close to charge neutrality), the I_{ph} in the HOIST was enhanced by ~966 times. Meanwhile, the response speed was not affected as shown in fig. S24.

Another remarkable feature of the HOIST is that the photoresponse extended deep into the channel (~25 μm away from the drain electrode in contrast to ~1 μm in WS_2, Fig. 4E). One possibility is the increase of exciton diffusion constant at high exciton density (*50*). However, in this scenario, the diffusion length is ~1 μm, which is still one order of magnitude lower than our observation. Another possible mechanism is the reduction of binding energy by dipolar screening (*51*), making excitons separable under modest electric field away from the electrodes. Quantitative modeling will require further theoretical efforts. Nevertheless, we demonstrated that ET

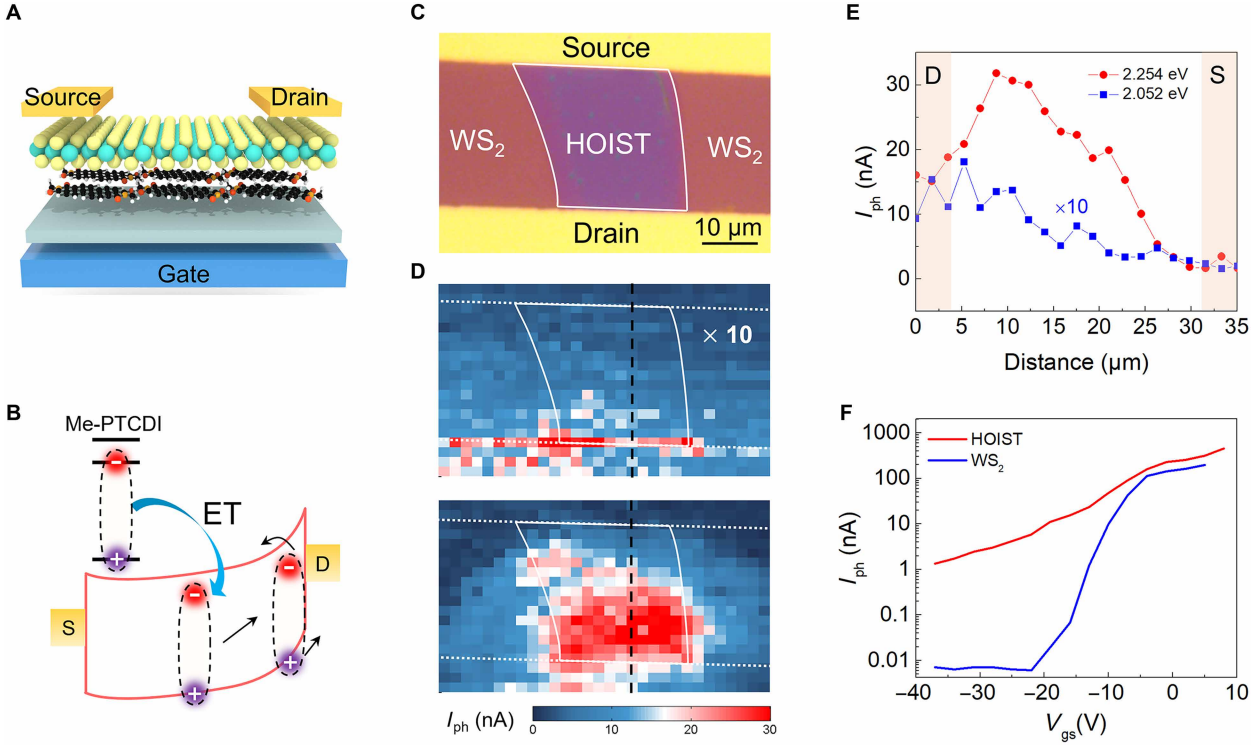

Fig. 4. HOIST phototransistors. (**A**) Schematic illustration of the phototransistor. (**B**) Band diagram of HOIST phototransistors under a bias voltage. (**C**) Optical micrograph of a typical device with both WS_2 and HOIST channel regions. Scale bar, 10 μm. (**D**) I_{ph} mapping of the device in (C) using 2.052 eV (top, multiplied by 10 times) and 2.254 eV (bottom) laser excitation. (**E**) I_{ph} spatial profile across the channel region in HOIST from the vertical line cuts in (D). The blue curve is multiplied by 10 for clarity. The positions of source and drain electrodes are marked. (**F**) I_{ph} as a function of V_g in the WS_2 (blue) and HOIST (red) channels under 2.254-eV laser excitation.

could enhance both the photoresponsivity and effective device area, both of which contributed to photocurrent extraction.

DISCUSSION

The observation of efficient ET in 2D HOIST opens enormous opportunities beyond conventional vdW heterostructures. For example, ET with complementary absorption spectrum through the Dexter mechanism may enable broadband optoelectronics. The ET enhancement in our work can outperform the other mechanism for enhancing the absorption in TMDC such as CT, plasmonic, and electronic structure modification (see table S3). In addition, the ET process provides an additional means to manipulate valley degree of freedom and exciton diffusion in TMDCs. Now, hundreds of organic materials (including small molecules, polymers, and covalently bonded frameworks) are known to adopt layered structure (*29*–*31*). With properly designed molecules and tandem structures, broadband absorption enhancement is within reach. Furthermore, combining the solution processability of organic materials and chemical vapor deposition of 2D materials, we can envision large-area HOIST array for image sensor and display applications.

MATERIALS AND METHODS

Sample and device preparations

WS_2 flakes and BN for encapsulation were fabricated by mechanically exfoliation using polydimethylsiloxane (PDMS), while the BN for Me-PTCDI growth was exfoliated on 300-nm SiO_2/Si substrate directly. Me-PTCDI crystals were obtained with vdW epitaxy growth on BN on 300-nm SiO_2/Si substrate in a home-built tube furnace. Then, the heterostructure was prepared with WS_2 and BN on PDMS transferred onto Me-PTCDI in the glove box sequentially. The photodetector was made by transferring two gold on the top of WS_2 as source and drain electrodes. For the TEM sample, instead of monolayers that are fragile during the milling process, thick Me-PTCDI and few-layer WS_2 are used to build the heterostructure, which would share the same interface quality and interlayer distances with the heterostructure of monolayer Me-PTCDI and monolayer WS_2. The sample is protected with 150-nm Au electrode and then covered with Pt using electron-beam evaporation before milling.

Optical and spectroscopic measurements

The PL images were collected using an optical microscope (Olympus BX51M). For the room temperature PL images, samples were illuminated by a 450-nm light-emitting diode (LED), and the PL images were collected by a colored charge-coupled device (CCD) camera. The excitation light was filtered by a long-pass filter in front of the CCD. For the low-temperature PL images, the sample was illuminated by a 500-nm LED.

For the low temperature PL test, samples were placed in cryostat chamber (OXFORD INSTRUMENTS_MicrostatHires) cooled by liquid nitrogen. A halogen lamp was connected with a monochromator to generate monochromatic light, which was used to excite samples. The PL signal was collected by 50× objective (numerical aperture = 0.7) and analyzed by a liquid nitrogen–cooled silicon CCD detector with a monochromator. For the PLE test, the wavelength is swept by controlling the monochromator by computer.

For the excitation polarization test, a polarizer was used to turn the monochromatic light to linear polarization light, and a half-waveplate was used to control the polarization of the incident light. For the PL polarization test, another polarizer was placed before the spectrometer to identify the polarization of PL for a given polarization of the incident light. To test the relationship between polarization degree and excitation energy in HOIST, PLE tests were performed at the polarization angle with the maximum intensity and minimum intensity, respectively. A 300 line/mm grating was used for the PL test with negligible polarization effect. The polarization effect of other optical elements in the light path is also ruled out by testing monolayer WS_2 showing no linear anisotropy, which is consistent with (*39*).

For the differential reflection contrast test, samples were illuminated with white light covering the spectral range from 450 to 900 nm. The refection from substrate ($R_{substrate}$) and sample (R_{sample}) were recorded, respectively. The differential reflection contrast was achieved by $(R_{sample} - R_{substrate})/R_{substrate}$.

Photodetector measurements

The measurements were carried out in the same cryostat chamber used for the low-temperature PL test. Keithley 2612 was used to apply the source-drain bias, while Keithley 2450 was used to apply the source-gate bias. A supercontinuum white-light laser source (Fianium WhiteLase SC400) and acousto-optic tunable filter were used to generate monochromatic light. For the photocurrent test, the laser was focused to a light spot around 1 μm. By changing the light spot position, pristine WS_2 and HOIST area in the same device were tested. For the photocurrent mapping, a motorized stage was used to change the sample position with photocurrent recorded.

First-principles calculations

Density functional calculations were performed using the local density approximation implemented in the Quantum Espresso package. The vacuum distance was set to be 30 Å between adjacent layers to avoid spurious interactions. The vdW interaction was included by the DFT-D2 method. We adopted an in-plane herringbone lattice structure for the monolayer Me-PTCDI. The geometric structure was relaxed until the force converges within 0.01 eV/Å. The layer distances were also checked using the Perdew-Burke-Ernzerhof (PBE) functional as implemented in the Vienna Ab initio Simulation Package. The GW and GW + BSE calculations were performed with the BerkeleyGW package. The dielectric matrix was constructed with a cutoff energy of 50 rydberg. The dielectric matrix and the self-energy were calculated on a 16 × 16 × 1 *k*-grid. The quasiparticle bandgap was converged to within 0.05 eV. In the calculation of optical absorption spectra, the quasiparticle band structure and electron-hole interaction kernel were interpolated onto a 96 × 96 × 1 fine k-grid, with the 1*s* exciton binding energy converged to within 0.05 eV.

ET rates estimation

The Dexter ET rates can be analytically expressed via the Fermi golden rule (*48*, *49*)

$$K = \frac{2\pi}{\hbar} \sum_A \sum_D \left| V\left(\phi_A^e, \phi_A^h, \psi_D^e, \psi_D^h\right) \right|^2 \delta\left(E_D - E_A\right) \quad (2)$$

with the exciton orbits ϕ_A^e ϕ_A^h of the TMDC monolayer as the acceptor and the excitonic states $\psi_D^e \psi_D^h$ of the molecule Me-PTCDI as the donor. The delta function makes sure that only energy-conserving

processes contribute. The exciton energy of 1*s* state of Me-PTCDI and the 2*s* state of WS_2 is nearly perfect aligned, suggesting large ET in this type heterostructure.

In the exchange Coulomb interaction V, which is determined by

$$V = \langle \phi^{*e}_A \psi^e_D | H_I | \phi^h_A \psi^{*h}_D \rangle \quad (3)$$

where H_I is the system Hamiltonian. The Coulomb interaction strength is determined by

$$H_I = \frac{e^2}{4\pi\epsilon(r-r')} \quad (4)$$

The screening dielectric constant ϵ is determined experimentally, with values of ~5.6 for Me-PTCDI/WS_2 and 6.0 for WS_2/MoS_2. Overall, the screening effect has only a minor influence on the transition rate between Me-PTCDI/WS_2 and WS_2/MoS_2, as the dielectric constants of the two heterostructures are relatively similar. Instead, the interlayer separation plays a more dominant role, as the Dexter transfer rate follows the relation $K_{\text{Dexter}} \sim e^{-\beta r}$, where β is a decay factor dependent on the wave function overlap and r is the interlayer distance—both of which are strongly correlated with the separation between layers.

For the case of exciton in our manuscript, V can be further derived as

$$V = \left\langle \Psi^{WS_2}_{2s} \Psi^{\text{Me-PTCDI}}_0 | H_I | \Psi^{WS_2}_0 \Psi^{\text{Me-PTCDI}}_{\text{Frenkel}} \right\rangle \quad (5)$$

$\Psi^{\text{Me-PTCDI}}_0$ and $\Psi^{WS_2}_0$ represent the ground states of the exciton in each layer of the bilayer system, respectively. $\Psi^{WS_2}_{2s}$ and $\Psi^{\text{Me-PTCDI}}_{\text{Frenkel}}$ is the exciton sate that is determined by

$$\Psi^{WS_2}_{2s} = \sum_{c\ v} A^{2s}_{cv} |c\rangle |v\rangle \quad (6)$$

$$\Psi^{\text{Me-PTCDI}}_{\text{Frenkel}} = \sum_{h\ l} A^{\text{Frenkel}}_{hl} |h\rangle |l\rangle \quad (7)$$

By solving the A^{2s}_{cv} and A^{Frenkel}_{hl} with the Bathe-Salpeter equation, from the Bathe-Salpeter-Equation using the BerkeleyGW package,

$$(E_c - E_v) A^S_{cv} + \sum_{v'c'} \left(K^{eh,d}_{vc,v'c'} + K^{eh,x}_{vc,v'c'} \right) A^S_{c'v'} = E_S A^S_{cv} \quad (8)$$

where the direct and exchange electron-hole interaction kernels are

$$K^{eh,d}_{vc,v'c'} = -\int dr dr' \psi^*_c(r) \psi_{c'}(r) \frac{e^2}{4\pi\epsilon |r-r'|} \psi_v(r') \psi^*_{v'}(r') \quad (9)$$

$$K^{eh,x}_{vc,v'c'} = \int dr dr' \psi^*_c(r) \psi_v(r) \frac{e^2}{4\pi\epsilon_0 |r-r'|} \psi_{c'}(r') \psi^*_{v'}(r') \quad (10)$$

the ET rate can be calculated by

$$K = \frac{2\pi}{\hbar} \left| \sum_{cv} \sum_{hl} \int dr \int dr' A^{2s}_{cv} A^{\text{Frenkel}}_{hl} \psi^*_v(r) \psi_h(r) \frac{e^2}{4\pi\epsilon(r-r')} \psi^*_l(r') \psi_c(r') \right|^2 \delta(E_{2s} - E_{\text{Frenkel}}) \quad (11)$$

Orbital wave function simulation

DFT calculations were performed using the generalized gradient approximation for the exchange-correlation potential, the projector-augmented wave method, and a plane wave basis set as implemented in the Vienna ab initio simulation package. A plane-wave basis set was used, with a kinetic energy cutoff of up to 400 eV applied consistently across all computations. For geometry optimization, the Heyd-Scuseria-Ernzerhof hybrid functional (HSE06) was used. Brillouin zone integration was carried out using a k-mesh of 15 × 15 × 1 for the 1 × 1 H-WS_2 monolayer and a coarser mesh of 2 × 1 × 1 for Me-PTCDI. During these optimizations, the shape and volume of each supercell were maintained at their respective monolayer values while allowing all atoms within the cell to relax until the residual forces on each atom were below 0.03 eV/Å. The heterostructure modeling the Me-PTCDI/WS_2 interface comprised a $5 \times 5\sqrt{3}$ WS_2 lattice and a 1 × 1 Me-PTCDI molecule, incorporating a 1% tensile strain on the WS_2 layer. In the electronic structure calculations, dispersion corrections were included at the DFT-D3 level using the PBE functional. For sampling the first Brillouin zone of the PTCDI/WS_2 heterostructure, a k-mesh of 2 × 1 × 1 was adopted.

Supplementary Materials

This PDF file includes:

Notes S1 to S3
Tables S1 to S4
Figs. S1 to S24
References

REFERENCES AND NOTES

1. P. Rivera, H. Yu, K. L. Seyler, N. P. Wilson, W. Yao, X. Xu, Interlayer valley excitons in heterobilayers of transition metal dichalcogenides. *Nat. Nanotechnol.* **13**, 1004–1015 (2018).
2. Y. Liu, N. O. Weiss, X. Duan, H.-C. Cheng, Y. Huang, X. Duan, Van der Waals heterostructures and devices. *Nat. Rev. Mater.* **1**, 16042 (2016).
3. F. Withers, O. Del Pozo-Zamudio, A. Mishchenko, A. P. Rooney, A. Gholinia, K. Watanabe, T. Taniguchi, S. J. Haigh, A. K. Geim, A. I. Tartakovskii, K. S. Novoselov, Light-emitting diodes by band-structure engineering in van der Waals heterostructures. *Nat. Mater.* **14**, 301–306 (2015).
4. X. Xiong, M. Huang, B. Hu, X. Li, F. Liu, S. Li, M. Tian, T. Li, J. Song, Y. Wu, A transverse tunnelling field-effect transistor made from a van der Waals heterostructure. *Nat. Electron.* **3**, 106–112 (2020).
5. D. Unuchek, A. Ciarrocchi, A. Avsar, K. Watanabe, T. Taniguchi, A. Kis, Room-temperature electrical control of exciton flux in a van der Waals heterostructure. *Nature* **560**, 340–344 (2018).
6. M. Achermann, M. A. Petruska, S. Kos, D. L. Smith, D. D. Koleske, V. I. Klimov, Energy-transfer pumping of semiconductor nanocrystals using an epitaxial quantum well. *Nature* **429**, 642–646 (2004).
7. M. Einzinger, T. Wu, J. F. Kompalla, H. L. Smith, C. F. Perkinson, L. Nienhaus, S. Wieghold, D. N. Congreve, A. Kahn, M. G. Bawendi, M. A. Baldo, Sensitization of silicon by singlet exciton fission in tetracene. *Nature* **571**, 90–94 (2019).
8. Q. Zhang, T. Atay, J. R. Tischler, M. S. Bradley, V. Bulović, A. V. Nurmikko, Highly efficient resonant coupling of optical excitations in hybrid organic/inorganic semiconductor nanostructures. *Nat. Nanotechnol.* **2**, 555–559 (2007).
9. G. Konstantatos, M. Badioli, L. Gaudreau, J. Osmond, M. Bernechea, F. P. G. de Arquer, F. Gatti, F. H. L. Koppens, Hybrid graphene–quantum dot phototransistors with ultrahigh gain. *Nat. Nanotechnol.* **7**, 363–368 (2012).
10. X. Chen, K. Shehzad, L. Gao, M. Long, H. Guo, S. Qin, X. Wang, F. Wang, Y. Shi, W. Hu, Y. Xu, X. Wang, Graphene hybrid structures for integrated and flexible optoelectronics. *Adv. Mater.* **32**, 1902039 (2020).
11. D. Kufer, I. Nikitskiy, T. Lasanta, G. Navickaite, F. H. L. L. Koppens, G. Konstantatos, Hybrid 2D–0D MoS_2–PbS quantum dot photodetectors. *Adv. Mater.* **27**, 176–180 (2015).
12. D. Kozawa, A. Carvalho, I. Verzhbitskiy, F. Giustiniano, Y. Miyauchi, S. Mouri, A. H. Castro Neto, K. Matsuda, G. Eda, Evidence for fast interlayer energy transfer in $MoSe_2$/WS_2 heterostructures. *Nano Lett.* **16**, 4087–4093 (2016).
13. L. Wu, Y. Chen, H. Zhou, H. Zhu, Ultrafast energy transfer of both bright and dark excitons in 2D van der Waals heterostructures beyond dipolar coupling. *ACS Nano* **13**, 2341–2348 (2019).
14. Z. Hu, P. L. Hernández-Martínez, X. Liu, M.-R. Amara, W. Zhao, K. Watanabe, T. Taniguchi, H. V. Demir, Q. Xiong, Trion-mediated Förster resonance energy transfer and optical gating effect in WS_2/hBN/$MoSe_2$ heterojunction. *ACS Nano* **14**, 13470–13477 (2020).
15. W. Xu, D. Kozawa, Y. Liu, Y. Sheng, K. Wei, V. B. Koman, S. Wang, X. Wang, T. Jiang, M. S. Strano, J. H. Warner, Determining the optimized interlayer separation distance in

vertical stacked 2D WS_2:hBN:MoS_2 heterostructures for exciton energy transfer. *Small* **14**, 1–10 (2018).
16. T. Yamaoka, H. E. Lim, S. Koirala, X. Wang, K. Shinokita, M. Maruyama, S. Okada, Y. Miyauchi, K. Matsuda, Efficient photocarrier transfer and effective photoluminescence enhancement in type I monolayer $MoTe_2$/WSe_2 heterostructure. *Adv. Funct. Mater.* **28**, 1801021 (2018).
17. X. Hong, J. Kim, S.-F. Shi, Y. Zhang, C. Jin, Y. Sun, S. Tongay, J. Wu, Y. Zhang, F. Wang, Ultrafast charge transfer in atomically thin MoS_2/WS_2 heterostructures. *Nat. Nanotechnol.* **9**, 682–686 (2014).
18. C. Jin, E. Y. Ma, O. Karni, E. C. Regan, F. Wang, T. F. Heinz, Ultrafast dynamics in van der Waals heterostructures. *Nat. Nanotechnol.* **13**, 994–1003 (2018).
19. V. M. Agranovich, Y. N. Gartstein, M. Litinskaya, Hybrid resonant organic-inorganic nanostructures for optoelectronic applications. *Chem. Rev.* **111**, 5179–5214 (2011).
20. D. Y. Qiu, F. H. Da Jornada, S. G. Louie, Optical spectrum of MoS_2: Many-body effects and diversity of exciton states. *Phys. Rev. Lett.* **111**, 119901 (2013).
21. J. Gu, X. Liu, E. Lin, Y. Lee, S. R. Forrest, V. M. Menon, Dipole-aligned energy transfer between excitons in two-dimensional transition metal dichalcogenide and organic semiconductor. *ACS Photonics* **5**, 100–104 (2018).
22. X. Liu, J. Gu, K. Ding, D. Fan, X. Hu, Y.-W. Tseng, Y.-H. Lee, V. Menon, S. R. Forrest, Photoresponse of an organic semiconductor/two-dimensional transition metal dichalcogenide heterojunction. *Nano Lett.* **17**, 3176–3181 (2017).
23. Y. L. Huang, Y. J. Zheng, Z. Song, D. Chi, A. T. S. Wee, S. Y. Quek, The organic-2D transition metal dichalcogenide heterointerface. *Chem. Soc. Rev.* **47**, 3241–3264 (2018).
24. J. Ji, J. H. Choi, Recent progress in 2D hybrid heterostructures from transition metal dichalcogenides and organic layers: Properties and applications in energy and optoelectronics fields. *Nanoscale* **14**, 10648–10689 (2022).
25. M. Gobbi, E. Orgiu, P. Samorì, When 2D materials meet molecules: Opportunities and challenges of hybrid organic/inorganic van der Waals heterostructures. *Adv. Mater.* **30**, 1706103 (2018).
26. Y. Guo, L. Wu, J. Deng, L. Zhou, W. Jiang, S. Lu, D. Huo, J. Ji, Y. Bai, X. Lin, S. Zhang, H. Xu, W. Ji, C. Zhang, Band alignment and interlayer hybridization in monolayer organic/WSe_2 heterojunction. *Nano Res* **15**, 1276–1281 (2022).
27. C. Wang, H. Dong, L. Jiang, W. Hu, Organic semiconductor crystals. *Chem. Soc. Rev.* **47**, 422–500 (2018).
28. F. Yang, S. Cheng, X. Zhang, X. Ren, R. Li, H. Dong, W. Hu, 2D organic materials for optoelectronic applications. *Adv. Mater.* **30**, 1702415 (2018).
29. Y. L. Shi, M. P. Zhuo, X. D. Wang, L. S. Liao, Two-dimensional organic semiconductor crystals for photonics applications. *ACS Appl. Nano Mater.* **3**, 1080–1097 (2020).
30. H. Zhao, Y. Zhao, Y. Song, M. Zhou, W. Lv, L. Tao, Y. Feng, B. Song, Y. Ma, J. Zhang, J. Xiao, Y. Wang, D. Lien, M. Amani, H. Kim, X. Chen, Z. Wu, Z. Ni, P. Wang, Y. Shi, H. Ma, X. Zhang, J. Xu, A. Troisi, A. Javey, X. Wang, Strong optical response and light emission from a monolayer molecular crystal. *Nat. Commun.* **10**, 5589 (2019).
31. D. He, Y. Zhang, Q. Wu, R. Xu, H. Nan, J. Liu, J. Yao, Z. Wang, S. Yuan, Y. Li, Y. Shi, J. Wang, Z. Ni, L. He, F. Miao, F. Song, H. Xu, K. Watanabe, T. Taniguchi, J.-B. Xu, X. Wang, Two-dimensional quasi-freestanding molecular crystals for high-performance organic field-effect transistors. *Nat. Commun.* **5**, 5162 (2014).
32. A. Chernikov, T. C. Berkelbach, H. M. Hill, A. Rigosi, Y. Li, O. B. Aslan, D. R. Reichman, M. S. Hybertsen, T. F. Heinz, Exciton binding energy and nonhydrogenic rydberg series in monolayer WS_2. *Phys. Rev. Lett.* **113**, 076802 (2014).
33. P. Rivera, J. R. Schaibley, A. M. Jones, J. S. Ross, S. Wu, G. Aivazian, P. Klement, K. Seyler, G. Clark, N. J. Ghimire, J. Yan, D. G. Mandrus, W. Yao, X. Xu, Observation of long-lived interlayer excitons in monolayer $MoSe_2$–WSe_2 heterostructures. *Nat. Commun.* **6**, 6242 (2015).
34. G. Moody, C. Kavir Dass, K. Hao, C.-H. Chen, L.-J. Li, A. Singh, K. Tran, G. Clark, X. Xu, G. Berghäuser, E. Malic, A. Knorr, X. Li, Intrinsic homogeneous linewidth and broadening mechanisms of excitons in monolayer transition metal dichalcogenides. *Nat. Commun.* **6**, 8315 (2015).
35. E. J. Sie, A. Steinhoff, C. Gies, C. H. Lui, Q. Ma, M. Rösner, G. Schönhoff, F. Jahnke, T. O. Wehling, Y. H. Lee, J. Kong, P. Jarillo-Herrero, N. Gedik, Observation of exciton redshift–blueshift crossover in monolayer WS_2. *Nano Lett.* **17**, 4210–4216 (2017).
36. F. Cadiz, E. Courtade, C. Robert, G. Wang, Y. Shen, H. Cai, T. Taniguchi, K. Watanabe, H. Carrere, D. Lagarde, M. Manca, T. Amand, P. Renucci, S. Tongay, X. Marie, B. Urbaszek, Excitonic linewidth approaching the homogeneous limit in MoS_2-based van der Waals heterostructures. *Phys. Rev. X* **7**, 1–10 (2017).
37. C. Zhang, Y. Zhang, Z. Fang, Y. Chen, Z. Chen, H. He, H. Zhu, Near-unity-efficiency energy transfer from perovskite to monolayer semiconductor through long-range migration and asymmetric interfacial transfer. *ACS Appl. Mater. Interfaces* **13**, 41895–41903 (2021).
38. S. Park, N. Mutz, S. A. Kovalenko, T. Schultz, D. Shin, A. Aljarb, L. Li, V. Tung, P. Amsalem, E. J. W. List-Kratochvil, J. Stähler, X. Xu, S. Blumstengel, N. Koch, Type-I energy level alignment at the PTCDA—Monolayer MoS_2 interface promotes resonance energy transfer and luminescence enhancement. *Adv. Sci.* **8**, 1–9 (2021).
39. C. Han, J. Ye, Polarized resonant emission of monolayer WS_2 coupled with plasmonic sawtooth nanoslit array. *Nat. Commun.* **11**, 713 (2020).
40. A. M. Jones, H. Yu, N. J. Ghimire, S. Wu, G. Aivazian, J. S. Ross, B. Zhao, J. Yan, D. G. Mandrus, D. Xiao, W. Yao, X. Xu, Optical generation of excitonic valley coherence in monolayer WSe_2. *Nat. Nanotechnol.* **8**, 634–638 (2013).
41. S. Kumar, I. S. Dunn, S. Deng, T. Zhu, Q. Zhao, O. F. Williams, R. Tempelaar, L. Huang, Exciton annihilation in molecular aggregates suppressed through quantum interference. *Nat. Chem.* **15**, 1118–1126 (2023).
42. D. L. Dexter, A theory of sensitized luminescence in solids. *J. Chem. Phys.* **21**, 836–850 (1953).
43. T. Förster, Zwischenmolekulare energiewanderung und fluoreszenz. *Ann. Phys.* **437**, 55–75 (1948).
44. N. Hildebrandt, How to Apply FRET: From Experimental Design to Data Analysis, in *FRET – Förster Resonance Energy Transfer* (Wiley, 2013); https://onlinelibrary.wiley.com/doi/abs/10.1002/9783527656028.ch05, pp. 105–163.
45. M. Palummo, M. Bernardi, J. C. Grossman, Exciton radiative lifetimes in two-dimensional transition metal dichalcogenides. *Nano Lett.* **15**, 2794–2800 (2015).
46. M. Amani, P. Taheri, R. Addou, G. H. Ahn, D. Kiriya, D.-H. Lien, J. W. Ager, R. M. Wallace, A. Javey, Recombination kinetics and effects of superacid treatment in sulfur- and selenium-based transition metal dichalcogenides. *Nano Lett.* **16**, 2786–2791 (2016).
47. S. Speiser, Photophysics and mechanisms of intramolecular electronic energy transfer in bichromophoric molecular systems: Solution and supersonic jet studies. *Chem. Rev.* **96**, 1953–1976 (1996).
48. E. Malic, H. Appel, O. T. Hofmann, A. Rubio, Förster-induced energy transfer in functionalized graphene. *J. Phys. Chem. C* **118**, 9283–9289 (2014).
49. Z.-Q. You, C.-P. Hsu, Theory and calculation for the electronic coupling in excitation energy transfer. *Int. J. Quantum Chem.* **114**, 102–115 (2014).
50. M. Kulig, J. Zipfel, P. Nagler, S. Blanter, C. Schüller, T. Korn, N. Paradiso, M. M. Glazov, A. Chernikov, Exciton diffusion and halo effects in monolayer semiconductors. *Phys. Rev. Lett.* **120**, 207401 (2018).
51. P. D. Cunningham, A. T. Hanbicki, K. M. McCreary, B. T. Jonker, Photoinduced bandgap renormalization and exciton binding energy reduction in WS_2. *ACS Nano* **11**, 12601–12608 (2017).
52. Q. Wang, S. You, B. Kobin, P. Amsalem, F. Zu, R. Wang, A. Opitz, S. Hecht, L. Chi, N. Koch, Terrylene on monolayer WS_2: Coverage-dependent molecular re-orientation and interfacial electronic energy levels. *Mater. Adv.* **5**, 9604–9612 (2024).
53. H. Shi, H. Pan, Y.-W. Zhang, B. I. Yakobson, Quasiparticle band structures and optical properties of strained monolayer MoS_2 and WS_2. *Phys. Rev. B* **87**, 155304 (2013).
54. C. Herbig, C. Zhang, F. Mujid, S. Xie, Z. Pedramrazi, J. Park, M. F. Crommie, Local electronic properties of coherent single-layer WS_2/WSe_2 lateral heterostructures. *Nano Lett.* **21**, 2363–2369 (2021).
55. A. F. Rigosi, H. M. Hill, K. T. Rim, G. W. Flynn, T. F. Heinz, Electronic band gaps and exciton binding energies in monolayer Mo_xW_{1-x}. *Phys. Rev. B* **94**, 075440 (2016).
56. D. R. T. Zahn, G. N. Gavrila, M. Gorgoi, The transport gap of organic semiconductors studied using the combination of direct and inverse photoemission. *Chem. Phys.* **325**, 99–112 (2006).
57. M. C. R. Delgado, E.-G. Kim, D. A. da S. Filho, J.-L. Bredas, Tuning the charge-transport parameters of perylene diimide single crystals via end and/or core functionalization: A density functional theory investigation. *J. Am. Chem. Soc.* **132**, 3375–3387 (2010).
58. L. Zhang, A. Sharma, Y. Zhu, Y. Zhang, B. Wang, M. Dong, H. T. Nguyen, Z. Wang, B. Wen, Y. Cao, B. Liu, X. Sun, J. Yang, Z. Li, A. Kar, Y. Shi, D. Macdonald, Z. Yu, X. Wang, Y. Lu, Efficient and layer-dependent exciton pumping across atomically thin organic–inorganic type-I heterostructures. *Adv. Mater.* **30**, (2018).
59. A. Karmakar, A. Al-Mahboob, C. E. Petoukhoff, O. Kravchyna, N. S. Chan, T. Taniguchi, K. Watanabe, K. M. Dani, Dominating interlayer resonant energy transfer in type-II 2D heterostructure. *ACS Nano* **16**, 3861–3869 (2022).
60. M. Dandu, R. Biswas, S. Das, S. Kallatt, S. Chatterjee, M. Mahajan, V. Raghunathan, K. Majumdar, Strong single- and two-photon luminescence enhancement by nonradiative energy transfer across layered heterostructure. *ACS Nano* **13**, 4795–4803 (2019).
61. C.-H. Cheng, Z. Li, A. Hambarde, P. B. Deotare, Efficient energy transfer across organic–2D inorganic heterointerfaces. *ACS Appl. Mater. Interfaces* **10**, 39336–39342 (2018).
62. M. Rahaman, E. Marino, A. G. Joly, C. E. Stevens, S. Song, A. Alfieri, Z. Jiang, B. T. O'Callahan, D. J. Rosen, K. Jo, G. Kim, J. R. Hendrickson, P. Z. El-Khoury, C. Murray, D. Jariwala, Tunable localized charge transfer excitons in nanoplatelet–2D chalcogenide van der Waals heterostructures. *ACS Nano* **18**, 15185–15193 (2024).
63. S. Singh, W. Gong, C. E. Stevens, J. Hou, A. Singh, H. Zhang, S. B. Anantharaman, A. D. Mohite, J. R. Hendrickson, Q. Yan, D. Jariwala, Valley-polarized interlayer excitons in 2D chalcogenide–halide perovskite–van der Waals heterostructures. *ACS Nano* **17**, 7487–7497 (2023).
64. W.-R. Syong, J.-H. Fu, Y.-H. Kuo, Y.-C. Chu, M. Hakami, T.-Y. Peng, J. Lynch, D. Jariwala, V. Tung, Y.-J. Lu, Enhanced photogating gain in scalable MoS_2 plasmonic photodetectors via resonant plasmonic metasurfaces. *ACS Nano* **18**, 5446–5456 (2024).

65. H.-Y. Lan, Y.-H. Hsieh, Z.-Y. Chiao, D. Jariwala, M.-H. Shih, T.-J. Yen, O. Hess, Y.-J. Lu, Gate-tunable plasmon-enhanced photodetection in a monolayer MoS_2 phototransistor with ultrahigh photoresponsivity. *Nano Lett.* **21**, 3083–3091 (2021).
66. A. Yang, J.-C. Blancon, W. Jiang, H. Zhang, J. Wong, E. Yan, Y.-R. Lin, J. Crochet, M. G. Kanatzidis, D. Jariwala, T. Low, A. D. Mohite, H. A. Atwater, Giant enhancement of photoluminescence emission in WS_2 -two-dimensional perovskite heterostructures. *Nano Lett.* **19**, 4852–4860 (2019).

Acknowledgments: We thank P. Ludwig Hernandez-Martinez and H. Volkan Demir for the numerical simulation of FRET rate. **Funding:** This work is supported by the National Key R&D Program of China (grant nos. 2021YFA1202900, 2022YFB4400100, 2023YFF1500500, and 2021YFA0715600), the Jiangsu Natural Science Foundation (grant no. BK20202005 , BK20232024, and BG2024017), the National Natural Science Foundation of China (grant nos. T2221003 and U24A20295), the Research Grant Council of Hong Kong (no. 15205619). X.C. is supported by the National Natural Science Foundation of China (grant no. 62104198) and the Fundamental Research Funds for the Central Universities (G2025KY05018). R.F. and L.Y. are supported by the National Science Foundation (NSF) grant no. DMR-2124934. X.W. acknowledges the support by the Yachen Foundation and the New Cornerstone Science Foundation through the XPLORER PRIZE. **Author contributions:** X.W. conceived the idea and supervised the project together with L.G. and X.G. X.C. and Huijuan Zhao. performed sample fabrication and optical measurements. Z.T contributed to the photodetector fabrication. R.F., C.H., J.Q., L.Y., and W.J. contributed to DFT calculations. C.S and Haiming Zhu. contributed to the transient absorption spectroscopy. Z.H, J.-B.X., L.W., and Y.S. contributed to data analysis. X.C., R.F., L.G. X.G., and X.W. cowrote the manuscript with input from other authors. All authors contributed to discussions. **Competing interests:** The authors declare that they have no competing interests. **Data and materials availability:** All data needed to evaluate the conclusions in the paper are present in the paper and/or the Supplementary Materials.

Submitted 31 January 2025
Accepted 5 August 2025
Published 5 September 2025
10.1126/sciadv.adw3969